A Novel Describing Function Small-Signal Modeling Approach for Passive Ripple Constant On-Time Controlled Converter With Exponentially Varying Slope

Yi-Rong Huang and Ching-Jan Chen, *Senior Member, IEEE*

***Abstract*—Passive ripple constant on-time (PRCOT) controlled converters have been widely used for mobile applications to improve light-load efficiency and transient response. An accurate small-signal model is inevitable for PRCOT control to estimate stability and design high loop gain bandwidth. The describing function (DF) method has been used to model the constant on-time control. However, previous research assumes a constant passive ripple slope, which is different at small RC time-constant conditions and causes inaccurate modeling results. In this article, a new DF modeling approach is proposed to handle exponentially varying slope. This article takes a PRCOT controlled boost converter as an example to demonstrate the modeling approach. Simulation and experiment results verified the accuracy of the proposed model even beyond the switching frequency for both constant slope or exponentially varying slope passive ramp cases.**

***Index Terms*—Constant on-time (COT) control, constant ripple slope, describing function (DF), passive ripple (PR), small-signal model.**

I. Introduction

THE passive ripple (PR) circuit for modulation ramp generation has been widely used in constant on-time (COT) and other controls for buck and boost converters in mobile applications due to its low quiescent current and fast transient response features [1], [2], [3], [4], [5], [6], [7], [8], [9], [10], [11], [12], [13], [14], [15], [16], [17]. For example, a boost converter with PR constant on-time control (PRCOT) is shown in Fig. 1. The PR is generated by connecting an *RC* circuit to a square wave voltage, synchronized with the duty signal *d*. The output voltage of PR exhibits a constant slope when the *RC* time constant is significantly larger than the switching period T_s, as depicted in Fig. 2(a). Conversely, the PR exhibits an exponentially varying slope when the RC time constant is close to T_s, as illustrated in Fig. 2(b). This exponentially varying slope situation often happens when the PR circuit is implemented into an integrated circuit (IC). To save the occupied area in IC for the PR circuit, smaller values of *RC* are usually chosen. Both the PR circuit and COT control can help to save the light-load efficiency for the power converter. COT control reduces switching frequency at light-load to reduce the switching loss. PR circuit has ultra-low current consumption. Instead of an active ramp circuit, a PR

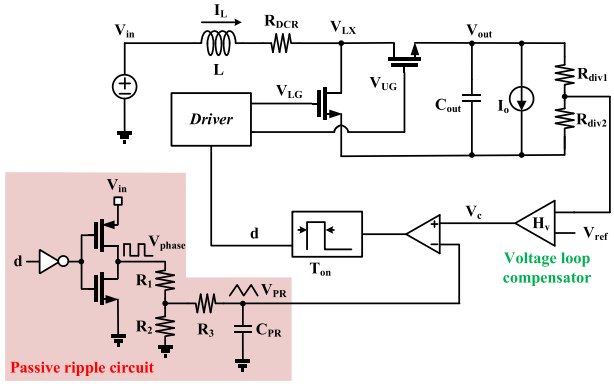

Fig. 1. Boost converter with PRCOT control.

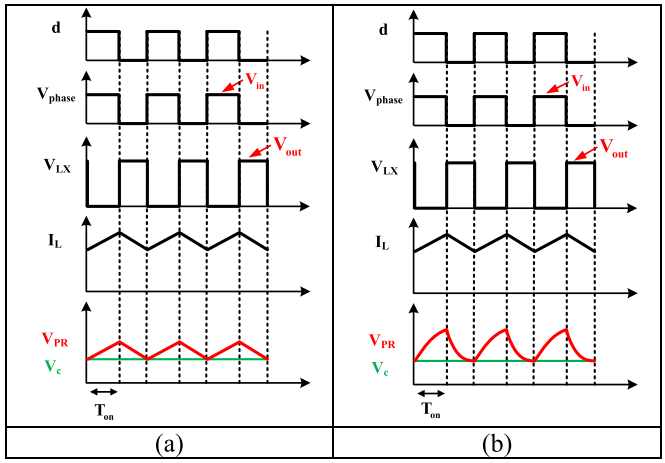

Fig. 2. Key waveforms of a boost converter with PRCOT control. (a) RC >> T_s. (b) RC ≈T_s.

Manuscript received 6 November 2023; revised 15 February 2024; accepted 28 March 2024. Date of publication 1 April 2024; date of current version 16 May 2024. This work was supported in part by Richtek Technology Corporation, Taiwan, and in part by the National Science and Technology Council, Taiwan. Recommended for publication by Associate Editor S. A. Khajehoddin. *(Corresponding author: Ching-Jan Chen.)*

The authors are with the Department of Electrical Engineering, National Taiwan University, Taipei 10617, Taiwan (e-mail: d09921001@ntu.edu.tw; chenjim@ntu.edu.tw).

Color versions of one or more figures in this article are available at https://doi.org/10.1109/TPEL.2024.3383855.

Digital Object Identifier 10.1109/TPEL.2024.3383855

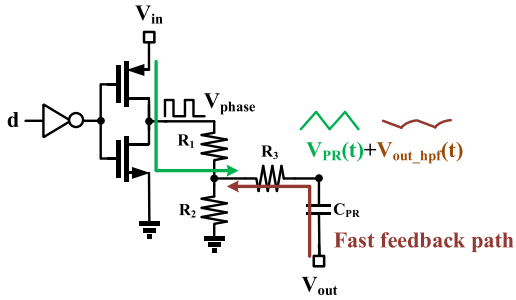

Fig. 3. PR circuit with fast feedback path connection.

circuit does not require active circuits such as an operational amplifier. Huang et al. [11] proposed a 240-nA quiescent current buck converter, and the control topology belongs to PRCOT control. Furthermore, a PR circuit can form a fast feedback path to improve transient performance by connecting the bottom of C_{PR} to v_{out} as shown in Fig. 3 [1], [2], [4], [5], [6], [7], [9], [11], [13]. This circuit can increase transient response without an active adder circuit. This control scheme is sometimes called quasi-V^2 control in previous research.

Although PRCOT has been proposed in previous research, an accurate small signal model for PRCOT controls with exponentially varying slope have yet to be developed. An accurate small-signal model is inevitable for PRCOT control to estimate stability and design high loop gain bandwidth. The main challenge in modeling PRCOT is the exponentially varying slope caused by the *RC* time constant being insufficiently larger than T_s, which affects the PR, as illustrated in Fig. 2(b).

Li and Lee describing function (DF) method [18] has been widely utilized to derive small signal model of COT controls [3], [19], [20], [21], [22], [23], [24], [25], [26], [27], [28], [29]. DF applies Fourier-series analysis to modulation waveform, which achieves good accuracy whether for constant- or variable-frequency control. Based on Li's DF method, [3], [27], and [28] have attempted to derive a small signal model for control with a PR circuit. However, Lin et al. [3], Lu et al. [27], and Huang and Cheung [28] make specific assumptions on PR, leading to inaccuracies in the derived model.

This article proposes a modeling method based on DF to derive a small signal model for PRCOT controlled converter with exponentially varying slope. Unlike Lin et al. [3], Lu et al. [27], and Huang and Cheung [28], the proposed approach does not make specific assumptions and achieve good accuracy in various *RC* time constant conditions. The PRCOT controlled boost converter, illustrated in Fig. 1, serves as an example circuit for model derivation. The v_c to v_{out} transfer function, $G_{vc}(s)$, is derived, and a pole-zero form for $G_{vc}(s)$ is obtained for system design. Both SIMPLIS simulation and experiment verified the developed $G_{vc}(s)$ model. Furthermore, previous methods [3], [27], and [28] are also used to derive PRCOT controlled boost converter, and compared with proposed method.

The article is organized as follows:

1) Section I: An introduction of PRCOT control and DF method are presented.
2) Section II: A new method is proposed to derive $G_{vc}(s)$ of a PRCOT controlled boost converter. For comparison, previous methods [3], [27], and [28] are also used to derive a controlled boost converter.
3) Section III: The developed models are verified and compared with SIMPLIS simulation and experimental results.
4) Section IV: Conclusion and the opportunities for extension of the proposed modeling method.

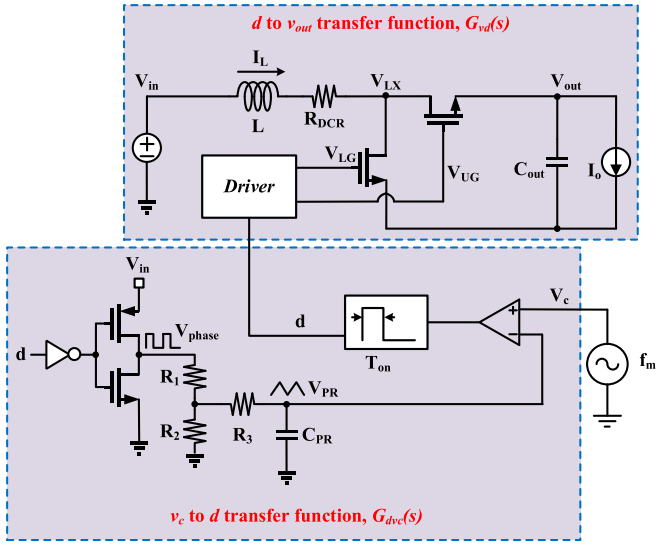

Fig. 4. Proposed modeling strategy.

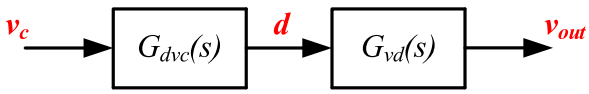

Fig. 5. Control block diagram of proposed modeling method.

II. Proposed Modeling Approach for Passive Ripple Constant On-Time Control With Exponentially Varying Slope

In this section, the proposed method, and previous methods [3], [27], and [28] are used to derive small signal models of PRCOT controlled boost converter. The proposed method is presented in Section II-A. The previous methods [3], [27] and [28] are presented in Section II-B. These derived models are verified and compared in Section III.

A. Derivation of $G_{vc}(s)$ By the Proposed Method

The modeling strategy to develop the transfer function from v_c to v_{out}, denoted by $G_{vc}(s)$, is shown in Fig. 4. We first cut the voltage loop compensator and then inject a sinusoidal perturbation with a small magnitude into the v_c signal. Fig. 5 shows that the control block diagram of the proposed modeling method only involves two control blocks: the transfer function from d to v_{out}, denoted by $G_{vd}(s)$, and the transfer function from v_c to d, represented by $G_{dvc}(s)$. The $G_{vc}(s)$ is obtained by multiplying $G_{vd}(s)$ and $G_{dvc}(s)$. The $G_{vd}(s)$ has been developed by average model as (1) and exhibits good accuracy [30]. The parameters are given in Table I, where R_{LG} and R_{UG} are the ON-resistance of power stage lower and upper switch, respectively. Therefore, in this section, we focus on developing the $G_{dvc}(s)$ transfer

TABLE I
TRANSFER FUNCTION PARAMETERS OF $G_{vd}(s)$

Item	Equation
K_{vd}	$\frac{\left((1-D)\cdot V_{out} - R_{DCR}\cdot\frac{I_o}{1-D} - R_{LG}\cdot\frac{I_o}{1-D}\right)}{(1-D)^2}$
ω_{RHP}	$\frac{(1-D)^2\cdot V_{out}}{L\cdot I_o} - \frac{R_{LG}}{L} - \frac{R_{DCR}}{L}$
ω_{o_vd}	$\frac{(1-D)}{\sqrt{L\cdot C_{out}}}$
Q_{o_vd}	$\frac{(1-D)}{R_{DCR}+(1-D)\cdot R_{UG}+D\cdot R_{LG}}\cdot\frac{\sqrt{L}}{\sqrt{C_{out}}}$
ω_{o_vc}	$\omega_{o\_vd}\cdot\sqrt{\frac{V_{out}+D\cdot K_{vd}}{V_{out}}}$

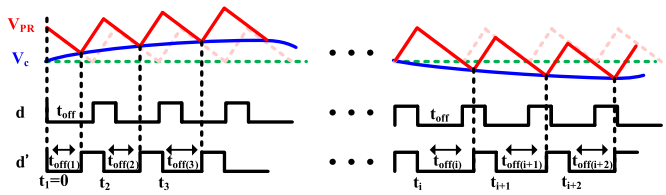

Fig. 6. Perturbated modulation waveform of PRCOT control.

function. It is worth mentioning that the inner PR loop has been included in $G_{dvc}(s)$

$$G_{vd}(s) = K_{vd}\cdot\frac{\left(1-\frac{s}{\omega_{\mathrm{RHP}}}\right)}{\left(1+\frac{s}{Q_{o\_vd}\cdot\omega_{o\_vd}}+\frac{s^2}{\omega_{o\_vd}^2}\right)}. \tag{1}$$

1) Step 1: Model Assumptions: There are two assumptions for the derivation: the magnitude of the perturbed sinusoidal wave is small enough and the switching frequency f_s and perturbation frequency f_m are commensurable, which means that $N\cdot f_s = M\cdot f_m$, where N and M are positive integers. It is worth mentioning that there is no assumption of a constant PR slope.

2) Step 2: Equations of Modulation Principle: By injecting sinusoidal perturbation into v_c, the equation of $v_c(t)$ is shown in (2). In (2), r_o is the dc value for a steady-state operating point. $\hat{r}$ is the magnitude and θ_o is the initial phase. Observing the perturbated modulation waveform of PRCOT control in Fig. 6, the sinusoidal wave of v_c causes different OFF-times. The equation for the off-time in every ith cycle can be presented as (3), where the t_{off} is the steady-state OFF-time value, and $\Delta t_{\mathrm{off}(i)}$ is the perturbated value for the ith cycle. From (3) and Fig. 6, the t_i can be calculated as (4). Using the modulation law, (5) can be obtained. In (5), it should be noted that $v_{\mathrm{PR}}(t_i + t_{\mathrm{off}(i)})$ has not been derived yet but will be derived in the next step. Li proposed (2)–(5) to derive the small signal model, and then several papers followed these steps [3], [19], [20], [21], [22], [23], [24], [25], [26], [27], [28]:

$$v_c(t) = r_o + \hat{r}_o\sin(2\pi f_m t - \theta_o) \tag{2}$$

$$t_{\mathrm{off}(i)} = t_{\mathrm{off}} + \Delta t_{\mathrm{off}(i)} \tag{3}$$

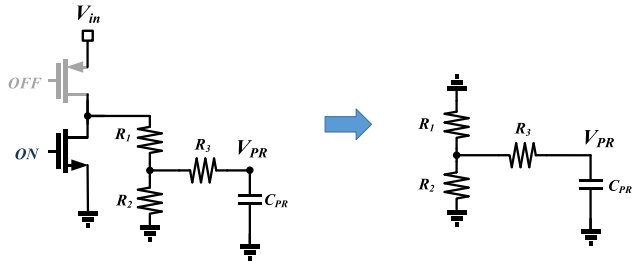

Fig. 7. PR equivalent circuit for t_i to $t_i + t_{\mathrm{off}(i)}$ interval.

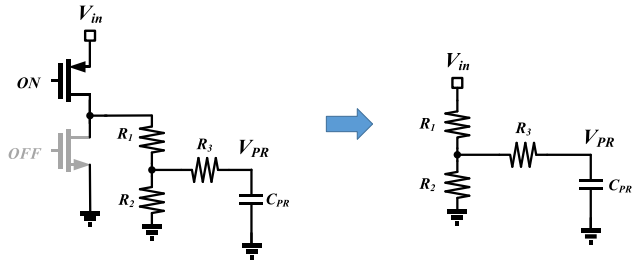

Fig. 8. PR equivalent circuit for $t_{i-1} + t_{\mathrm{off}(i-1)}$ to t_i interval.

$$t_i = (i-1)(t_{\mathrm{on}} + t_{\mathrm{off}}) + \sum_{k=1}^{i-1}\Delta t_{\mathrm{off(k)}} \tag{4}$$

$$v_c(t_i + t_{\mathrm{off}(i)}) = v_{PR}(t_i + t_{\mathrm{off}(i)}). \tag{5}$$

In this article, an additional (6) for $\Delta t_{\mathrm{off}}(t)$ is proposed to derive a small signal model, and this additional equation is the key point to handle the exponential mathematics. We know that the off-time $t_{\mathrm{off}(i)}$ is perturbated by sinusoidal function $v_c(t)$ with perturbation frequency f_m. Therefore, the $\Delta t_{\mathrm{off}}(t)$ varies as a sinusoidal function with perturbation frequency f_m. We can express $\Delta t_{\mathrm{off}}(t)$ as a sine function in (6), where $\hat{r}_{t\mathrm{off}}$ is the magnitude and $\theta_{t\mathrm{off}}$ is the initial phase. By (6), $\Delta t_{\mathrm{off}(i)}$ can be obtained as (7). By (4) and (7), (8) can be obtained. Equation (8) can be approximated as (9) because $\Delta t_{\mathrm{off}(k)}$ is much smaller than $t_{\mathrm{on}} + t_{\mathrm{off}}$. Equations (2), (5), and (9) are used to derive model in subsequent steps

$$\Delta t_{\mathrm{off}}(t) = \hat{r}_{t_{\mathrm{off}}}\sin(2\pi f_m t - \theta_{t_{\mathrm{off}}}) \tag{6}$$

$$\Delta t_{\mathrm{off}(i)} = \hat{r}_{t_{\mathrm{off}}}\sin(2\pi f_m(t_i + t_{\mathrm{off}(i)}) - \theta_{t_{\mathrm{off}}}) \tag{7}$$

$$\Delta t_{\mathrm{off}(i)} = \hat{r}_{t_{\mathrm{off}}}\sin\Big(2\pi f_m\big((i-1)T_s + t_{\mathrm{off}} + \sum_{k=1}^{i}\Delta t_{\mathrm{off}(k)}\big) - \theta_{t_{\mathrm{off}}}\Big) \tag{8}$$

$$\Delta t_{\mathrm{off}(i)} \approx \hat{r}_{t_{\mathrm{off}}}\sin(2\pi f_m\left((i-1)T_s + t_{\mathrm{off}}\right) - \theta_{t_{\mathrm{off}}}) \tag{9}$$

3) Step 3: Equations of Passive Ripple: In this step, $v_{\mathrm{PR}}(t_i + t_{\mathrm{off}(i)})$ in (5) is derived by deriving the differential equations of the PR equivalent circuits. The PR equivalent circuit for time interval t_i to $t_{\mathrm{off}(i)}$ is shown in Fig. 7. By the equivalent circuit, the differential equation of $v_{\mathrm{PR}}(t)$ *for* t_i *to* $t_i + t_{\mathrm{off}(i)}$ time interval can be obtained as (10). By solving differential (10), $v_{\mathrm{PR}}(t_i + t_{\mathrm{off}(i)})$ can be obtained as (11). By observing (11), it can be seen that $v_{\mathrm{PR}}(t_i)$ still need to be solved. In order to derive $v_{\mathrm{PR}}(t_i)$, the PR equivalent circuit for $t_{i-1} + t_{\mathrm{off}(i-1)}$ *to* t_i time interval is

shown in Fig. 8. The differential equation of $v_{\mathrm{PR}}(t)$ *for* $t_{i\text{-}1} + t_{\mathrm{off}(i\text{-}1)}$ *to* t_i time interval can be obtained as (12). By solving differential (12), $v_{\mathrm{PR}}(t_i)$ can be obtained as (13). Substituting (13) into (11), (14) can be obtained as

$$R_{\mathrm{eq}}C_{\mathrm{PR}}\frac{dv_{\mathrm{PR}}(t)}{dt} + v_{\mathrm{PR}}(t) = 0 \tag{10}$$

where

$$R_{\mathrm{eq}} = \frac{R_1R_2 + R_1R_3 + R_2R_3}{R_1 + R_2}$$

$$v_{\mathrm{PR}}(t_i + t_{\mathrm{off}(i)}) = e^{-\frac{t_{\mathrm{off}} + \Delta t_{\mathrm{off}(i)}}{R_{\mathrm{eq}}C_{\mathrm{PR}}}} \cdot v_{\mathrm{PR}}(t_i). \tag{11}$$

$$R_{\mathrm{eq}}C_{\mathrm{PR}}\frac{dv_{\mathrm{PR}}(t)}{dt} + v_{\mathrm{PR}}(t) = \frac{R_2}{R_1 + R_2} \cdot V_{\mathrm{in}} \tag{12}$$

$$v_{\mathrm{PR}}(t_i) = e^{\frac{-t_{\mathrm{on}}}{R_{\mathrm{eq}}C_{\mathrm{PR}}}} \cdot v_{\mathrm{PR}}(t_{i-1} + t_{\mathrm{off(i-1)}}) + \left(1 - e^{\frac{-t_{\mathrm{on}}}{R_{\mathrm{eq}}C_{\mathrm{PR}}}}\right)\frac{R_2}{R_1 + R_2}V_{\mathrm{in}} \tag{13}$$

$$v_{\mathrm{PR}}(t_i + t_{\mathrm{off}(i)}) = + e^{\frac{-T_s}{R_{\mathrm{eq}}C_{\mathrm{PR}}}} \cdot e^{\frac{-\Delta t_{\mathrm{off}(i)}}{R_{\mathrm{eq}}C_{\mathrm{PR}}}} \cdot v_{\mathrm{PR}}(t_{i-1} + t_{\mathrm{off(i-1)}}) + e^{\frac{-t_{\mathrm{off}}}{R_{\mathrm{eq}}C_{\mathrm{PR}}}} e^{\frac{-\Delta t_{\mathrm{off}(i)}}{R_{\mathrm{eq}}C_{\mathrm{PR}}}} \cdot \left(1 - e^{\frac{-t_{\mathrm{on}}}{R_{\mathrm{eq}}C_{\mathrm{PR}}}}\right) \times \frac{R_2}{R_1 + R_2}V_{\mathrm{in}}. \tag{14}$$

By observing (14), we can see that $v_{\mathrm{PR}}(t_i + t_{\mathrm{off}(i)})$ is dependent on $v_{\mathrm{PR}}(t_{i\text{-}1} + t_{\mathrm{off}(i\text{-}1)})$, which is the previous cycle value as $v_{\mathrm{PR}}(t_i + t_{\mathrm{off}(i)})$. Therefore, in order to obtain the complete information of $v_{\mathrm{PR}}(t_i + t_{\mathrm{off}(i)})$, we need to iterate $v_{\mathrm{PR}}(t_i + t_{\mathrm{off}(i)})$ back to $v_{\mathrm{PR}}(t_0 + t_{\mathrm{off}(0)})$, where $t_0 + t_{\mathrm{off}(0)}$ represents the start time. By iterating back to $v_{\mathrm{PR}}(t_0 + t_{\mathrm{off}(0)})$, (15) can be obtained. By Taylor approximation, (16) and (17) can be obtained. By substituting (16) and (17) into (15), (15) can be approximated to (18). Equation (18) is used to derive $G_{vc}(s)$ in the subsequent steps, and it is worth mentioning that (18) is too complicated to be derived with Li's deriving process

$$\begin{aligned} v_{\mathrm{PR}}(t_i + t_{\mathrm{off}(i)}) = & \\ & + e^{\frac{-iT_s}{R_{\mathrm{eq}}C_{\mathrm{PR}}}} \cdot e^{-\frac{\sum_{k=1}^{i}\Delta t_{\mathrm{off}(k)}}{R_{\mathrm{eq}}C_{\mathrm{PR}}}} \cdot v_{\mathrm{PR}}(t_0 + t_{\mathrm{off}(0)}) \\ & + e^{\frac{-t_{\mathrm{off}}}{R_{\mathrm{eq}}C_{\mathrm{PR}}}}\left(1 - e^{\frac{-t_{\mathrm{on}}}{R_{\mathrm{eq}}C_{\mathrm{PR}}}}\right)\frac{R_2}{R_1 + R_2} \cdot V_{\mathrm{in}} \\ & \cdot \sum_{k=1}^{i} e^{-\frac{(i-k)T_s}{R_{\mathrm{eq}}C_{\mathrm{PR}}}} \cdot e^{-\frac{\sum_{k}^{i}\Delta t_{\mathrm{off}(k)}}{R_{\mathrm{eq}}C_{\mathrm{PR}}}} \end{aligned} \tag{15}$$

$$e^{-\frac{\sum_{k=1}^{i}\Delta t_{\mathrm{off}(k)}}{R_{\mathrm{eq}}C_{\mathrm{PR}}}} \approx 1 - \frac{\sum_{k=1}^{i}\Delta t_{\mathrm{off}(k)}}{R_{\mathrm{eq}}C_{\mathrm{PR}}} \tag{16}$$

$$e^{-\frac{\sum_{k}^{i}\Delta t_{\mathrm{off}(k)}}{R_{\mathrm{eq}}C_{\mathrm{PR}}}} \approx 1 - \frac{\sum_{k}^{i}\Delta t_{\mathrm{off}(k)}}{R_{\mathrm{eq}}C_{\mathrm{PR}}} \tag{17}$$

$$\begin{aligned} v_{\mathrm{PR}}(t_i + t_{\mathrm{off}(i)}) \approx & \\ & + e^{\frac{-iT_s}{R_{\mathrm{eq}}C_{\mathrm{PR}}}} \cdot \left(1 - \frac{\sum_{k=1}^{i}\Delta t_{\mathrm{off}(k)}}{R_{\mathrm{eq}}C_{\mathrm{PR}}}\right) \cdot v_{\mathrm{PR}}(t_0 + t_{\mathrm{off}(0)}) \\ & + e^{\frac{-t_{\mathrm{off}}}{R_{\mathrm{eq}}C_{\mathrm{PR}}}}\left(1 - e^{\frac{-t_{\mathrm{on}}}{R_{\mathrm{eq}}C_{\mathrm{PR}}}}\right)\frac{R_2}{R_1 + R_2} \cdot V_{\mathrm{in}} \\ & \cdot \sum_{k=1}^{i} e^{-\frac{(i-k)T_s}{R_{\mathrm{eq}}C_{\mathrm{PR}}}} \cdot \left(1 - \frac{\sum_{k}^{i}\Delta t_{\mathrm{off}(k)}}{R_{\mathrm{eq}}C_{\mathrm{PR}}}\right). \end{aligned} \tag{18}$$

4) Step 4: Fourier Analysis: The perturbated duty cycle can be expressed as (19). Fourier analysis derives the Fourier coefficient of duty cycle $c_{m(d)}$ as shown in (20). Based on (20), (21) can be derived. It can be found that (21) contains $\hat{r}_{\mathrm{toff}}e^{-j\theta_{\mathrm{toff}}}$, so we have to find the relation between $\hat{r}_{\mathrm{toff}}e^{-j\theta_{\mathrm{toff}}}$ and $\hat{r}_o e^{-j\theta_o}$

$$\begin{aligned} & d(t)|_{0\le t\le t_M + t_{\mathrm{off(M)}} + t_{\mathrm{on}}} \\ & = \sum_{i=1}^{M}\left[u(t - t_i - t_{\mathrm{off}(i)}) - u(t - t_i - t_{\mathrm{off}(i)} - t_{\mathrm{on}})\right] \end{aligned} \tag{19}$$

$$c_{m(d)} = j\frac{2 \cdot f_m}{N}\int_0^{t_M + t_{\mathrm{off(M)}} + t_{\mathrm{on}}} d(t) \cdot e^{-j2\pi f_m t}dt \tag{20}$$

$$c_{m(d)} = f_s(1 - e^{-j2\pi f_m t_{\mathrm{on}}}) \cdot \frac{e^{j2\pi f_m \cdot T_s}}{1 - e^{j(2\pi f_m \cdot T_s)}} \cdot \hat{r}_{\mathrm{toff}}e^{-j\theta_{\mathrm{toff}}}. \tag{21}$$

In order to derive the relation between $\hat{r}_{\mathrm{toff}}e^{-j\theta_{\mathrm{toff}}}$ and $\hat{r}_o e^{-j\theta_o}$. We utilize the modulation law in (5) and the derived v_{PR} in (18) to present (22) shown at the bottom of the next page. By observing (22), it can be found that the left side contains sin-function of $v_c(t)$ and the right side contains sine function of $\Delta t_{\mathrm{off}(i)}$. Therefore, we can obtain the relation between $\hat{r}_{\mathrm{toff}}e^{-j\theta_{\mathrm{toff}}}$ and $\hat{r}_o e^{-j\theta_o}$ by applying Digital Fourier Transform to (22). By applying digital Fourier transform to (22), the relation between $\hat{r}_{\mathrm{toff}}e^{-j\theta_{\mathrm{toff}}}$ and $\hat{r}_o e^{-j\theta_o}$ can be derived as (23) shown at the bottom of the next page. By substituting (23) into (21), (24) shown at the bottom of the next page, can be obtained. Finally, based on (24) and (25) shown at the bottom of the next page, the v_c to d transfer function $G_{dvc}(s)$ can be obtained as (26) shown at the bottom of the next page.

5) Step 5: Pole-Zero Decomposition of $\mathrm{G_{dvc\,(s)}}$*:* In order to have a pole-zero form of (26), the padé approximation is applied to e^{sT_s} and $e^{-sT_{\mathrm{on}}}$ as shown in (27) and (28). This approximation is valid up to $1/(2T_s)$ [18]. By substituting (27) and (28) into (26), the pole-zero form of $G_{dvc}(s)$, denoted by $G_{dvc\_pz}(s)$ can be obtained as (29). It can be seen that $G_{dvc\_pz}(s)$ contains a complex pole with its frequency related to T_{on}, and two zeros with its frequency related to the time constant of PR circuit

$$e^{sT_s} \approx 1 + \frac{s \cdot T_s}{1 - \frac{s}{\frac{2}{\pi}\cdot\frac{\pi}{T_s}} + \frac{s^2}{\left(\frac{\pi}{T_s}\right)^2}} \tag{27}$$

$$e^{-s\cdot T_{\mathrm{on}}} \approx 1 - \frac{s \cdot T_{\mathrm{on}}}{1 + \frac{s}{\frac{2}{\pi}\cdot\frac{\pi}{T_{\mathrm{on}}}} + \frac{s^2}{\left(\frac{\pi}{T_{\mathrm{on}}}\right)^2}} \tag{28}$$

$$G_{dvc_{pz}}(s) = K_{dvc} \cdot \frac{\left(1 + \frac{s}{\omega_{\mathrm{PR}}}\right)\left(1 + \frac{s}{\omega_{\mathrm{PR_{HF}}}}\right)}{\left(1 + \frac{s}{Q_n\cdot\omega_n} + \frac{s^2}{\omega_n^2}\right)}. \tag{29}$$

The parameters are given in Table II.

6) Step 6: Derivation of $\mathrm{G}_{vc}\mathrm{(s)}$*:* Finally, the v_c to v_{out} transfer function, $G_{vc}(s)$, can be obtained by multiplying $G_{vd}(s)$ in

(1) and $G_{dvc}(s)$ in (26) as (30). The pole-zero form of $G_{vc}(s)$, denoted by $G_{vc\_pz}(s)$, can be obtained by multiplying (1) and (29) as (31). The parameters are summarized in Tables I and II.

Furthermore, it is worth noting that if the power stage is a buck converter, the $G_{dvc}(s)$ is the same as boost converter. Therefore, we can directly replace the $G_{vd}(s)$ of the boost converter with the $G_{vd}(s)$ of buck converter to derive PRCOT controlled buck converter

$$G_{vc}(s) = G_{vd}(s) \cdot G_{dvc}(s) \tag{30}$$

$$G_{vc\_pz}(s) = K_{vd} \cdot K_{dvc} \cdot \frac{\left(1-\frac{s}{\omega_{\mathrm{RHP}}}\right)\cdot\left(1+\frac{s}{\omega_{\mathrm{PR}}}\right)\cdot\left(1+\frac{s}{\omega_{\mathrm{PR_{HF}}}}\right)}{\left(1+\frac{s}{Q_{o_{vd}}\cdot\omega_{o_{vd}}}+\frac{s^2}{\omega_{o_{vd}}^2}\right)\cdot\left(1+\frac{s}{Q_n\cdot\omega_n}+\frac{s^2}{\omega_n^2}\right)}. \tag{31}$$

B. Derivation of $G_{dvc}(s)$ By Previous Method [3], [27], and [28]

The disparity between proposed and previous methods is evident in $G_{dvc}(s)$, because $G_{vd}(s)$ is the same. Therefore, we are going to derive $G_{dvc}(s)$ for comparison.

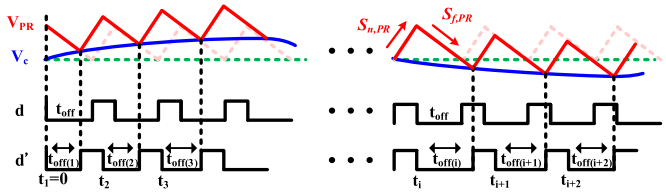

Fig. 9. Perturbated modulation waveform with constant PR slope.

In [3] and [27], the constant slope of PR is assumed. The modulation waveform with v_c perturbated is depicted in Fig. 9. By Fig. 9, the equation of the modulation principle is obtained as (32). The derivation of constant slope $S_{n,\mathrm{PR}}$, and $S_{f,\mathrm{PR}}$, can be referred to [17]. It can be observed that the constant slope of PR is utilized in (32). By using (32), the $\Delta t_{\mathrm{off}(i)}$ can be derived, as given in (33).

By applying Fourier-series analysis to duty signal, d, as (34), (35) can be derived. By substituting (33) into (35), the Fourier coefficient of duty can be derived as (36). The Fourier coefficient of v_c has been derived in (25). By (36) and (25), the control to duty transfer function can be derived as (37)

$$v_c(t_{i-1}+t_{\mathrm{off(i-1)}}) + s_{n,PR}t_{\mathrm{on}} = v_c(t_i + T_{\mathrm{off}(i)}) + s_{f,PR}t_{\mathrm{off}(i)} \tag{32}$$

$$\begin{aligned}
&\left(\hat{r}_o \sin(2\pi f_m((i-1)\cdot T_s + t_{\mathrm{off}}) - \theta_o) - \hat{r}_o \sin(2\pi f_m((i-2)\cdot T_s + t_{\mathrm{off}}) - \theta_o)\right) \\
&\quad - e^{\frac{-T_s}{R_{\mathrm{eq}}C_{\mathrm{PR}}}}\left(\hat{r}_o \sin(2\pi f_m((i-2)\cdot T_s + t_{\mathrm{off}}) - \theta_o) - \hat{r}_o \sin(2\pi f_m((i-3)\cdot T_s + t_{\mathrm{off}}) - \theta_o)\right) \\
&= e^{\frac{-(i)T_s}{R_{\mathrm{eq}}C_{\mathrm{PR}}}}\left(-\frac{v_{\mathrm{PR}}\left(t_0 + t_{off(0)}\right)}{R_{\mathrm{eq}}C_{\mathrm{PR}}} + \frac{e^{\frac{-t_{\mathrm{off}}}{R_{\mathrm{eq}}C_{\mathrm{PR}}}}}{1-e^{\frac{-T_s}{R_{\mathrm{eq}}C_{\mathrm{PR}}}}}\cdot\left(1-e^{\frac{-t_{\mathrm{on}}}{R_{\mathrm{eq}}C_{\mathrm{PR}}}}\right)\frac{\frac{R_2}{R_1+R_2}\cdot V_{\mathrm{in}}}{R_{\mathrm{eq}}C_{\mathrm{PR}}}\right)\cdot \hat{r}_{t_{\mathrm{off}}}\sin(2\pi f_m((i-1)T_s + t_{\mathrm{off}}) - \theta_{t_{\mathrm{off}}}) \\
&\quad - e^{\frac{-t_{\mathrm{off}}}{R_{\mathrm{eq}}C_{\mathrm{PR}}}}\frac{1}{1-e^{\frac{-T_s}{R_{\mathrm{eq}}C_{\mathrm{PR}}}}}\cdot\left(1-e^{\frac{-t_{\mathrm{on}}}{R_{\mathrm{eq}}C_{\mathrm{PR}}}}\right)\frac{\frac{R_2}{R_1+R_2}\cdot V_{\mathrm{in}}}{R_{\mathrm{eq}}C_{\mathrm{PR}}}\cdot \hat{r}_{t_{\mathrm{off}}}\sin(2\pi f_m((i-1)T_s + t_{\mathrm{off}}) - \theta_{t_{\mathrm{off}}}) \\
&\quad - e^{\frac{-(i-1)T_s}{R_{\mathrm{eq}}C_{\mathrm{PR}}}}\left(-\frac{v_{\mathrm{PR}}\left(t_0 + t_{off(0)}\right)}{R_{\mathrm{eq}}C_{\mathrm{PR}}} + \frac{e^{\frac{-t_{\mathrm{off}}}{R_{\mathrm{eq}}C_{\mathrm{PR}}}}}{1-e^{\frac{-T_s}{R_{\mathrm{eq}}C_{\mathrm{PR}}}}}\cdot\left(1-e^{\frac{-t_{\mathrm{on}}}{R_{\mathrm{eq}}C_{\mathrm{PR}}}}\right)\frac{\frac{R_2}{R_1+R_2}\cdot V_{\mathrm{in}}}{R_{\mathrm{eq}}C_{\mathrm{PR}}}\right)\cdot \hat{r}_{t_{\mathrm{off}}}\sin(2\pi f_m((i-2)T_s + t_{\mathrm{off}}) - \theta_{t_{\mathrm{off}}}) \\
&\quad + e^{\frac{-t_{\mathrm{off}}}{R_{\mathrm{eq}}C_{\mathrm{PR}}}}\frac{1}{1-e^{\frac{-T_s}{R_{\mathrm{eq}}C_{\mathrm{PR}}}}}\cdot\left(1-e^{\frac{-t_{\mathrm{on}}}{R_{\mathrm{eq}}C_{\mathrm{PR}}}}\right)\frac{\frac{R_2}{R_1+R_2}\cdot V_{\mathrm{in}}}{R_{\mathrm{eq}}C_{\mathrm{PR}}}\cdot \hat{r}_{t_{\mathrm{off}}}\sin(2\pi f_m((i-2)T_s + t_{\mathrm{off}}) - \theta_{t_{\mathrm{off}}})
\end{aligned} \tag{22}$$

$$\hat{r}_{t_{\mathrm{off}}}\, e^{-j\theta_{t_{\mathrm{off}}}} = \frac{\left(1-e^{\frac{-T_s}{R_{\mathrm{eq}}C_{\mathrm{PR}}}}\right)\cdot\left(1-e^{\frac{-T_s}{RC}}\cdot e^{-j(2\pi f_m\cdot T_s)}\right)}{-e^{\frac{-t_{\mathrm{off}}}{R_{\mathrm{eq}}C_{\mathrm{PR}}}}\cdot\left(1-e^{\frac{-t_{\mathrm{on}}}{R_{\mathrm{eq}}C_{\mathrm{PR}}}}\right)\frac{\frac{R_2}{R_1+R_2}\cdot V_{\mathrm{in}}}{R_{\mathrm{eq}}C_{\mathrm{PR}}}}\cdot \hat{r}_o e^{-j\theta_o} \tag{23}$$

$$c_{m(d)} = f_s\left(1-e^{-j2\pi f_m t_{\mathrm{on}}}\right)\cdot\frac{\left(1-e^{\frac{-T_s}{R_{\mathrm{eq}}C_{\mathrm{PR}}}}\right)\cdot\left(e^{\frac{-T_s}{RC}}-e^{j2\pi f_m\cdot T_s}\right)}{e^{\frac{-t_{\mathrm{off}}}{R_{\mathrm{eq}}C_{\mathrm{PR}}}}\cdot\left(1-e^{\frac{-t_{\mathrm{on}}}{R_{\mathrm{eq}}C_{\mathrm{PR}}}}\right)\frac{\frac{R_2}{R_1+R_2}\cdot V_{\mathrm{in}}}{R_{\mathrm{eq}}C_{\mathrm{PR}}}\cdot\left(1-e^{j(2\pi f_m\cdot T_s)}\right)}\cdot \hat{r}_o e^{-j\theta_o} \tag{24}$$

$$c_{m(v_c)} = j\frac{2\cdot f_m}{N}\int_0^{t_M+t_{\mathrm{off}(M)}+t_{\mathrm{on}}}\left(r_o + \hat{r}_o\sin(2\pi f_m t - \theta_o)\right)\cdot e^{-j2\pi f_m t}dt = \hat{r}_o\, e^{-j\theta_o} \tag{25}$$

$$G_{dvc}(s) \equiv \frac{c_{m(d)}}{c_{m(v_c)}} = f_s\left(1-e^{-s\cdot t_{\mathrm{on}}}\right)\cdot\frac{\left(1-e^{\frac{-T_s}{R_{\mathrm{eq}}C_{\mathrm{PR}}}}\right)\cdot\left(e^{\frac{-T_s}{RC}}-e^{s\cdot T_s}\right)}{e^{\frac{-t_{\mathrm{off}}}{R_{\mathrm{eq}}C_{\mathrm{PR}}}}\cdot\left(1-e^{\frac{-t_{\mathrm{on}}}{R_{\mathrm{eq}}C_{\mathrm{PR}}}}\right)\frac{\frac{R_2}{R_1+R_2}\cdot V_{\mathrm{in}}}{R_{\mathrm{eq}}C_{\mathrm{PR}}}\cdot\left(1-e^{s\cdot T_s}\right)} \tag{26}$$

TABLE II
TRANSFER FUNCTION PARAMETERS OF $G_{\mathrm{dvc\_pz}}(s)$

Item	Parameters
K_{dvc}	$f_s \frac{T_{on}}{T_s} \cdot \frac{\left(1-e^{\frac{-T_s}{R_{eq}C_{PR}}}\right)^2}{e^{\frac{-t_{off}}{R_{eq}C_{PR}}}\left(1-e^{\frac{-t_{on}}{R_{eq}C_{PR}}}\right)\frac{1}{R_{eq}C_{PR}}\frac{R_2}{R_1+R_2}V_{in}}$
ω_{PR}	$-\frac{\pi^2}{T_s}\frac{\left(\frac{e^{\frac{-T_s}{R_{eq}C_{PR}}}+1}{e^{\frac{-T_s}{R_{eq}C_{PR}}}-1}\right)\left(1-\sqrt{1-\frac{16}{\pi^2}\cdot\frac{(e^{\frac{-T_s}{R_{eq}C_{PR}}}-1)^2}{(e^{\frac{-T_s}{R_{eq}C_{PR}}}+1)^2}}\right)}{4}$
ω_{PR_HF}	$-\frac{\pi^2}{T_s}\frac{\left(\frac{e^{\frac{-T_s}{R_{eq}C_{PR}}}+1}{e^{\frac{-T_s}{R_{eq}C_{PR}}}-1}\right)\left(1+\sqrt{1-\frac{16}{\pi^2}\cdot\frac{(e^{\frac{-T_s}{R_{eq}C_{PR}}}-1)^2}{(e^{\frac{-T_s}{R_{eq}C_{PR}}}+1)^2}}\right)}{4}$
Q_n	$\frac{2}{\pi}$
ω_n	$\frac{\pi}{T_{on}}$

where

$$v_c(t) = r_o + \hat{r}_o \sin(2\pi f_m t - \theta_o)$$

$$t_{\mathrm{off}(i)} = t_{\mathrm{off}} + \Delta t_{\mathrm{off}(i)}$$

$$t_i = (i-1)(t_{\mathrm{on}} + t_{\mathrm{off}}) + \sum_{k=1}^{i-1} \Delta t_{\mathrm{off(k)}}$$

$$S_{n,PR} = \frac{1}{R_{\mathrm{EQ}} C_{\mathrm{PR}}} \frac{R_2}{R_1+R_2} \cdot (1-D) \cdot V_{\mathrm{in}}$$

$$S_{f,PR} = \frac{1}{R_{\mathrm{EQ}} C_{\mathrm{PR}}} \cdot \frac{R_2}{R_1+R_2} \cdot D \cdot V_{\mathrm{in}}$$

$$\Delta t_{\mathrm{off}(i)} = -2\frac{\hat{r}_o}{s_{f,PR}} \sin(\pi f_m T_s) \times \cos\left(2\pi f_m \left((i-1)T_s - \frac{t_{\mathrm{on}} - t_{\mathrm{off}}}{2}\right) - \theta_o\right) \tag{33}$$

$$c_{m(d)} = j\frac{2 \cdot f_m}{N} \int_0^{t_M + t_{\mathrm{off(M)}} + t_{\mathrm{on}}} d(t) \cdot e^{-j2\pi f_m t} dt \tag{34}$$

where

$$d(t)|_{0 \le t \le t_M + t_{\mathrm{off(M)}} + t_{\mathrm{on}}} = \sum_{i=1}^{M} \left[u(t - t_i - t_{\mathrm{off}(i)}) - u(t - t_i - t_{\mathrm{off}(i)} - t_{\mathrm{on}})\right]$$

$$c_{m(d)} = -\frac{j2\pi f_m}{N\pi} e^{-j2\pi f_m t_{\mathrm{off}}} (1 - e^{-j2\pi f_m t_{\mathrm{on}}}) \times \sum_{i=1}^{M} \left[e^{-j2\pi f_m (i-1) \cdot T_s} \sum_{k=1}^{i} \Delta t_{\mathrm{off(k)}}\right] \tag{35}$$

$$c_{m(d)} = \frac{f_s}{s_{f,PR}} (1 - e^{-j2\pi f_m t_{\mathrm{on}}}) \cdot \hat{r}_o e^{-j\theta_o} \tag{36}$$

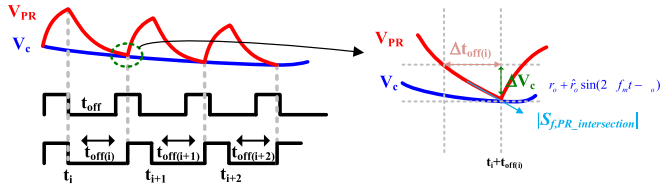

Fig. 10. Expanded view of perturbated modulation waveform.

$$G_{dvc\_\mathrm{constant\_slope}}(s) \equiv \frac{c_{m(d)}}{c_{m(v_c)}} = \frac{f_s}{s_{f,\mathrm{PR}}}(1 - e^{-j2\pi f_m t_{\mathrm{on}}}). \tag{37}$$

On the other hand, [28] attempts to address the exponential slope of PR by utilizing the slope when PR V_{PR} intersects with the control signal V_c as $S_{f,\mathrm{PR\_intersection}}$, depicted in Fig. 10. By differential equations of PR circuit in (10) and (12), the $S_{f,\mathrm{PR\_intersection}}$ can be derived as (38). By Fig. 10, the $\Delta t_{\mathrm{off}(i)}$ can be derived as (39).

By applying Fourier-series analysis to duty signal, d, as (40), (41) can be derived. By substituting (39) into (41), the Fourier coefficient of duty can be derived as (42). The Fourier coefficient of v_c has been derived in (25). By (42) and (25), the control to duty transfer function can be derived as (43)

$$|S_{f,\mathrm{PR\_intersection}}| = +\frac{1}{R_{\mathrm{eq}} C_{\mathrm{PR}}} \left(+e^{\frac{-T_S}{R_{\mathrm{eq}} C_{\mathrm{PR}}}} \cdot \left(V_c - \frac{R_2}{R_1+R_2} \cdot V_{\mathrm{in}}\right) + e^{\frac{-t_{\mathrm{off}}}{R_{\mathrm{eq}} C_{\mathrm{PR}}}} \frac{R_2}{R_1+R_2} \cdot V_{\mathrm{in}}\right) \tag{38}$$

$$\Delta t_{\mathrm{off}(i)} = \frac{\Delta V_c}{|S_{f,\mathrm{PR\_intersection}}|} = \frac{-\hat{r}_o \sin(2\pi f_m (t_i + t_{\mathrm{off}(i)}) - \theta_o)}{|S_{f,\mathrm{PR\_intersection}}|} \tag{39}$$

$$c_{m(d)} = j\frac{2 \cdot f_m}{N} \int_0^{t_M + t_{\mathrm{off(M)}} + t_{\mathrm{on}}} d(t) \cdot e^{-j2\pi f_m t} dt \tag{40}$$

where

$$d(t)|_{0 \le t \le t_M + t_{\mathrm{off(M)}} + t_{\mathrm{on}}} = \sum_{i=1}^{M} \left[u(t - t_i - t_{\mathrm{off}(i)}) - u(t - t_i - t_{\mathrm{off}(i)} - t_{\mathrm{on}})\right]$$

$$c_{m(d)} = -\frac{j2\pi f_m}{N\pi} e^{-j2\pi f_m t_{\mathrm{off}}} (1 - e^{-j2\pi f_m t_{\mathrm{on}}}) \times \sum_{i=1}^{M} \left[e^{-j2\pi f_m (i-1) \cdot T_s} \sum_{k=1}^{i} \Delta t_{\mathrm{off(k)}}\right] \tag{41}$$

$$c_{m(d)} = -\frac{f_s}{|S_{f,\mathrm{PR\_intersection}}|} \times (1 - e^{-j2\pi f_m t_{\mathrm{on}}}) \frac{e^{j2\pi f_m \cdot T_s}}{1 - e^{j2\pi f_m T_s}} \hat{r}_o e^{-j\theta_o} \tag{42}$$

TABLE III
CIRCUIT PARAMETERS OF THE SIMULATION

Item	Value	
Input voltage V_{in}	3.3 V	
Output voltage V_{out}	5 V	
Output current I_o	1 A	
Switching frequency f_s	200 kHz	
Inductor L	8.8 μH	
Inductor dc Resistor R_{DCR}	114 mΩ	
Output capacitor C_{out}	40 μF	
Low side power MOS turn-on Resistance R_{LG}	20 mΩ	
High side power MOS turn-on Resistance R_{UG}	20 mΩ	
PR circuit resistor R_1	560 Ω	
PR circuit resistor R_2	560 Ω	
PR circuit resistor R_3	820 Ω	
PR circuit capacitor C_{PR}	10 nF	1 nF

$$G_{dvc\_\text{intersection\_slope}}(s) \equiv \frac{c_{m(d)}}{c_{m(v_c)}}$$

$$= -\frac{f_s}{|S_{f,\text{PR\_intersection}}|}(1 - e^{-j2\pi f_m t_{on}})\frac{e^{j2\pi f_m \cdot T_s}}{1 - e^{j2\pi f_m T_s}}. \quad (43)$$

We summarize the differences in derivation between the proposed method and Li's methods [3], [27], [28] as follows:

1) *Expression of* $\Delta t_{off}(t)$*:* In the proposed method, $\Delta t_{off}(t)$ is expressed as a general sine function as (6), whereas Li's method employs a modulation law for deriving $\Delta t_{off}(t)$ as (33) and (39).
2) *Derivation of Modulation Ramp:* The proposed method employs a differential equation to express the modulation ramp, which is a PR in this example. In contrast, Li's method assumes a constant ramp slope, such as a constant PR slope in [3], [27], and a constant intersection slope in [28].

III. SIMULATION AND MEASUREMENT RESULTS

SIMPLIS simulation tools are used to verify the derived models. In previous research, the SIMPLIS behavior circuit has proved its accuracy in predicting small-signal behavior [3], [19], [20], [21], [22], [23], [24], [25], [26]. The organization is as follows: The proposed models (26), (29), (30), (31) and previous method models (37),(43) are verified by simulation in subsection A. Measurement results are used to verify the proposed model (26), (29), (30), (31) in Section III-B.

A. Simulation Verification

The circuit parameters and working conditions are given in Table III. It is worth mentioning that with the parameters provided in Table III and the change of C_{PR} from 10 to 1 nF, the value of $T_s/R_{eq}C_{PR}$ becomes approximately 4.5. Thus, the PR already exhibits an exponentially varying slope, as shown in Fig. 11.

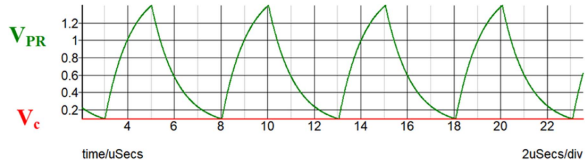

Fig. 11. Simulated modulation waveform with PR exhibiting exponentially varying slope ($T_s/R_{eq}C_{PR} = 4.5$).

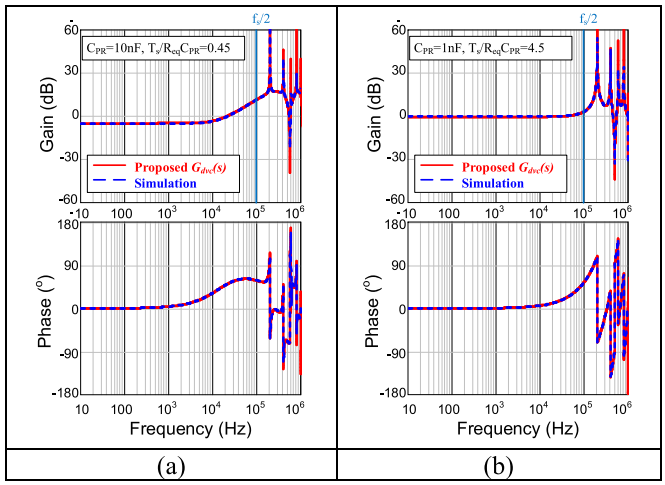

Fig. 12. Model verification of $G_{dvc}(s)$. (a) $C_{PR} = 10$ nF and $T_s/R_{eq}C_{PR} = 0.45$. (b) $C_{PR} = 1$nF and $T_s/R_{eq}C_{PR} = 4.5$.

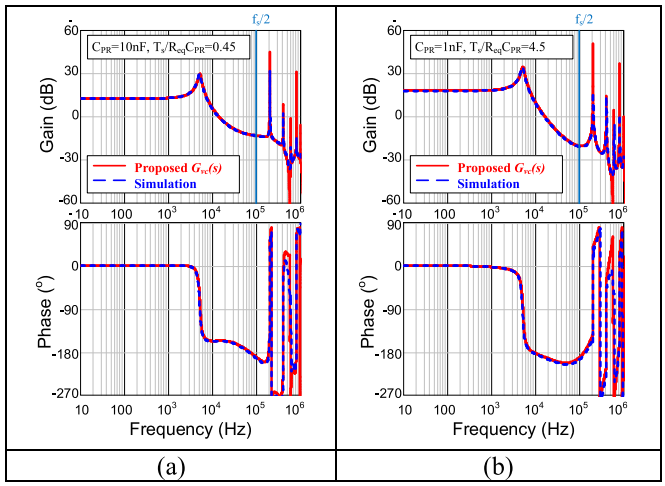

Fig. 13. Model verification of $G_{vc}(s)$. (a) $C_{PR} = 10$ nF and $T_s/R_{eq}C_{PR} = 0.45$. (b) $C_{PR} = 1$nF and $T_s/R_{eq}C_{PR} = 4.5$.

As can be seen from Figs. 12 and 13, the proposed model in (26) and (30) well matches with the simulation even beyond the switching frequency. Simplified transfer functions in (29) and (31) match the simulation up to half of switching frequency, as shown in Figs. 14 and 15.

Previous modeling methods with constant slopes in (37) and (43) are verified as depicted in Fig. 16. In Fig. 16, (43), $G_{dvc\_\text{intersection\_slope}}(s)$, fails to match with the simulation under the condition of $T_s/R_{eq}C_{PR} = 0.45$, but matches under the condition of $T_s/R_{eq}C_{PR} = 4.5$. In

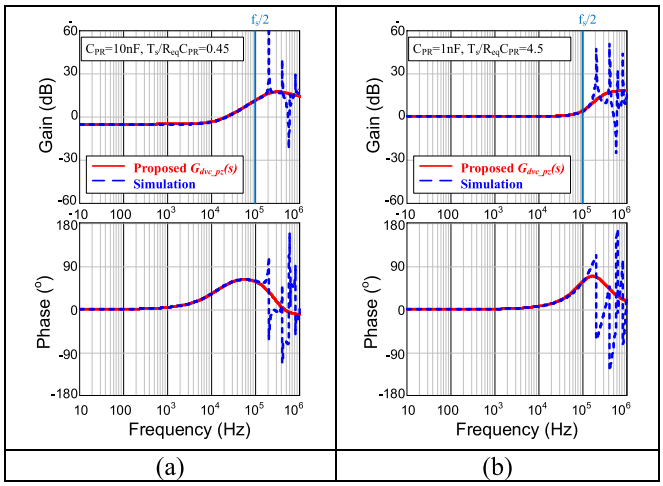

Fig. 14. Model verification of $G_{dvc\_pz}(s)$. (a) $C_{\rm PR} = 10$ nF and $T_s/R_{\rm eq}C_{\rm PR} = 0.45$. (b) $C_{\rm PR} = 1$nF and $T_s/R_{\rm eq}C_{\rm PR} = 4.5$.

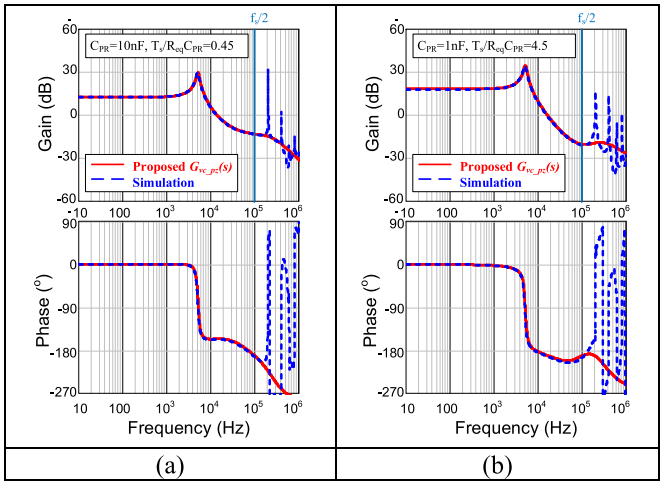

Fig. 15. Model verification of $G_{vc\_pz}(s)$. (a) $C_{\rm PR} = 10$ nF and $T_s/{\rm R}_{\rm eq}C_{\rm PR} = 0.45$. (b) $C_{\rm PR} = 1$nF and $T_s/R_{\rm eq}C_{\rm PR} = 4.5$.

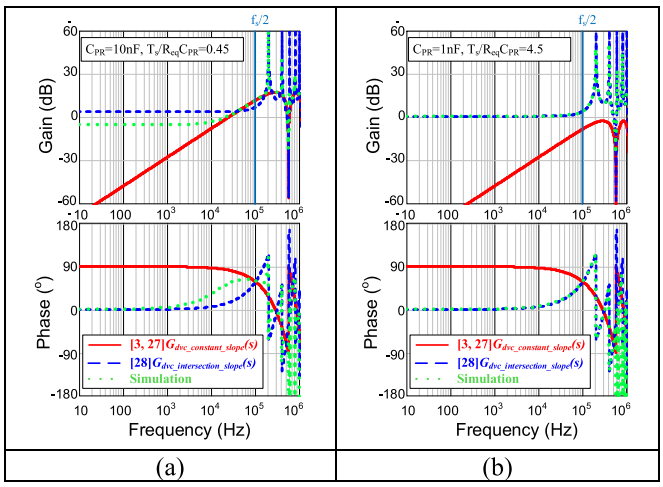

Fig. 16. Model verification of $G_{dvc\_{\rm constant\_slope}}(s)$ and $G_{dvc\_{\rm intersection\_slope}}(s)$. (a) $C_{\rm PR} = 10$ nF and $T_s/R_{\rm eq}C_{\rm PR} = 0.45$. (b) $C_{\rm PR} = 1$nF and $T_s/R_{\rm eq}C_{\rm PR} = 4.5$.

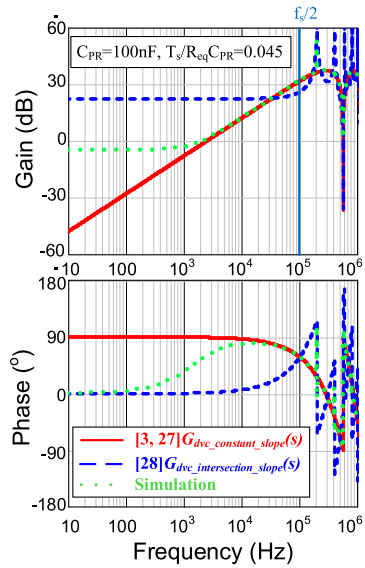

Fig. 17. Model verification of $G_{dvc\_{\rm constant\_slope}}(s)$ and $G_{dvc\_{\rm intersection\_slope}}(s)$ with $C_{\rm PR} = 100$ nF, $T_s/R_{\rm eq}C_{\rm PR} = 0.045$.

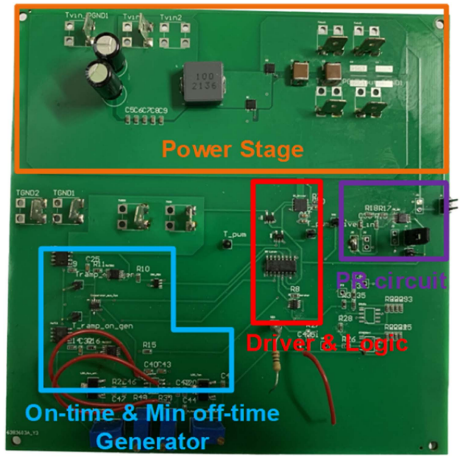

Fig. 18. Hardware photograph of a boost converter with PRCOT control.

Fig. 16, (37), $G_{dvc\_{\rm constant\_slope}}(s)$ fails to match with the simulation under the condition of $T_s/R_{\rm eq}C_{\rm PR} = 4.5$, but (37) begins to align with the simulation as $T_s/R_{\rm eq}C_{\rm PR}$ decreases. As depicted in Fig. 17, (37) more closely aligns with the simulation under small $T_s/R_{\rm eq}C_{\rm PR}$. Theoretically, (37) requires $T_s/R_{\rm eq}C_{\rm PR}$ to be equal to zero to match the simulation.

Table IV gives the comparison among the proposed methods [3], [27], and [28]. It can be seen that the proposed method can cover all T_s/RC ranges.

B. Experimental Verification

A boost converter with PRCOT control was implemented to verify the proposed model. The hardware photo of the implemented circuit is shown in Fig. 18, where discrete components

TABLE IV
COMPARISON AMONG PROPOSED MODEL, METHOD [3], [27], AND METHOD [28]

	Proposed method	Lin et al. [3], Lu et al. [27]	Huang and Cheung [28]
Method	Proposed DF	Li's DF	Li's DF
Specific assumption	X	Constant slope	Constant intersection slope
Model-Matched T_s/RC range	All range	Small T_s/RC	Large T_s/RC

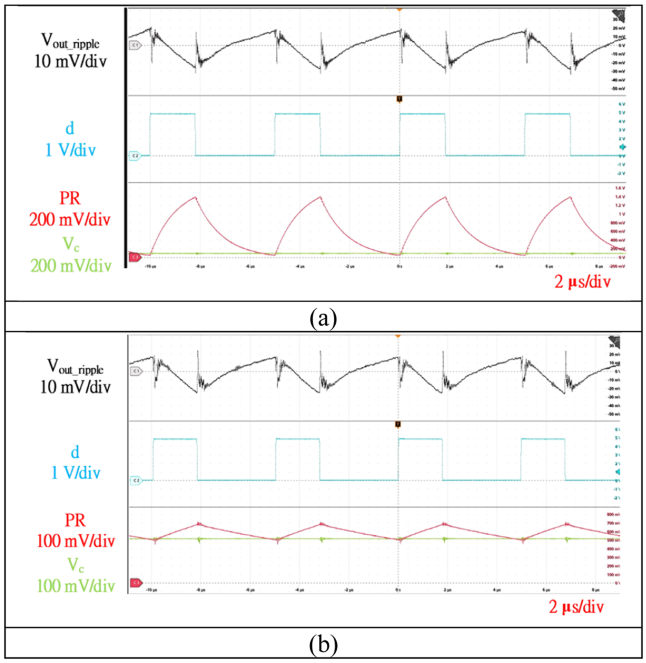

Fig. 19. Measured steady-state waveforms of boost converter with PRCOT control. (a) $C_{\rm PR} = 1$ nF. (b) $C_{\rm PR} = 10$ nF.

implement the PR circuit, on-time generator, and driver circuit. The working conditions and circuit parameters are given in Table III. The key steady-state waveforms are shown in Fig. 19(a) and (b). It can be seen that two test cases with different $C_{\rm PR}$ are measured, where smaller $C_{\rm PR}$ results in exponentially varying slope and larger $C_{\rm PR}$ results in a near constant slope in the passive ramp.

Fig. 20(a) and (b) show that the proposed v_c to $v_{\rm out}$ transfer function $G_{vc}(s)$ in (30) well matches with SIMPLIS simulation and experiment results even beyond the switching frequency for both $C_{\rm PR}$ cases. Therefore, the accuracy of the proposed modeling approach is proved for PRCOT control with constant slope passive ramp or exponentially varying slope.

More conditions are provided to verify the accuracy of $G_{vc}(s)$ in (30), including different $V_{\rm out}$ and $V_{\rm in}$, different I_o and different f_s as depicted in Figs. 21, 22, and 23. It can be seen that (30) still matches with SIMPLIS simulation and experiment results.

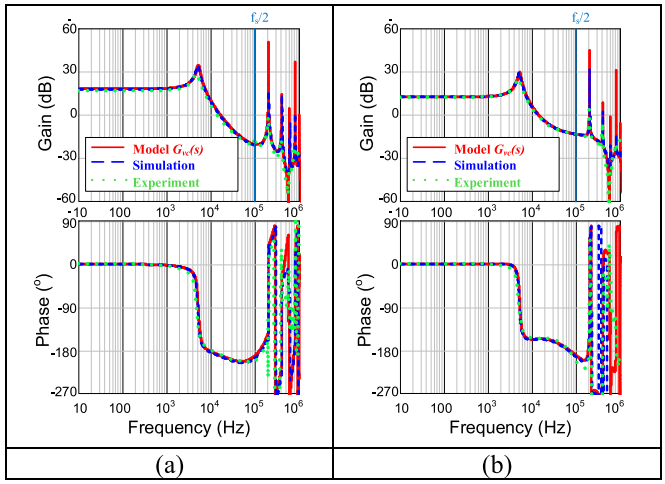

Fig. 20. Verification of $Gvc(s)$ by SIMPLIS simulation and measurement results. (a) $C_{\rm PR} = 1$ nF. (b) $C_{\rm PR} = 10$ nF.

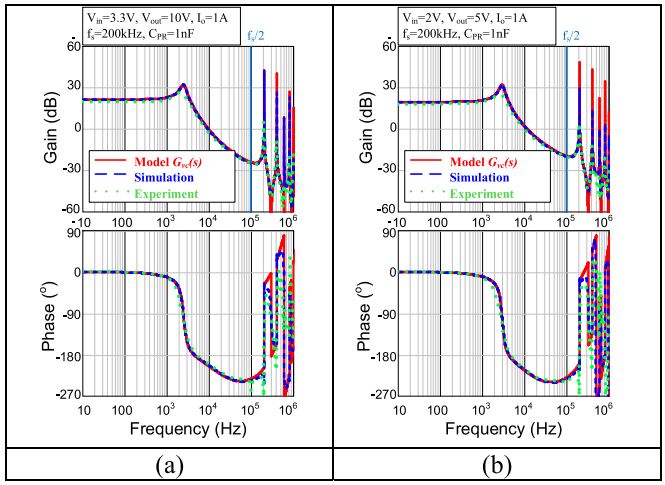

Fig. 21. Verification of $G_{vc}(s)$ for different $V_{\rm out}$ and $V_{\rm in}$. (a) $V_{\rm out} = 10$ V. (b)$V_{\rm in} = 2$ V.

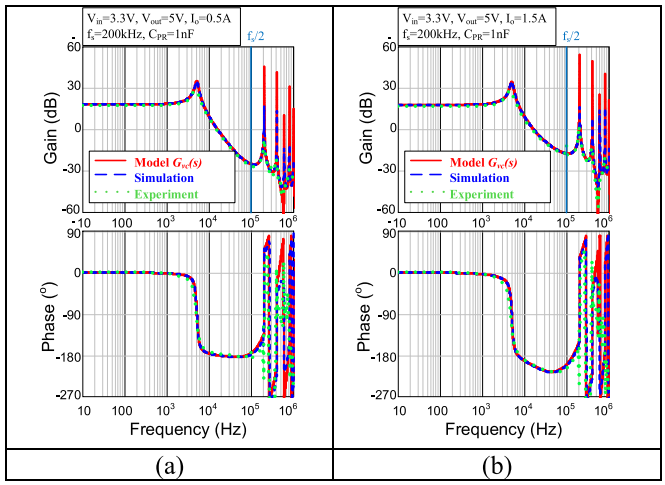

Fig. 22. Verification of $G_{vc}(s)$ for different output current. (a) $I_o = 0.5$ A. (b) $I_o = 1.5$A.

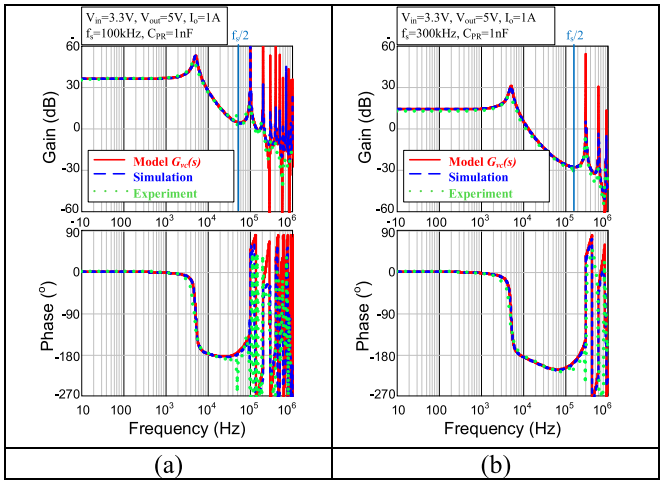

Fig. 23. Verification of $G_{vc}(s)$ for different switching frequency. (a) $f_s = 100$ kHz. (b) $f_s = 300$ kHz.

IV. Conclusion

A new DF modeling approach is proposed to improve model accuracy of PRCOT control with an exponentially varying slope of the passive ramp. The proposed model uses differential equations to describe the nonlinear modulation ramp, which obtains high accuracy and reality of circuit behavior. The v_c to $v_{\rm out}$ transfer function, $G_{vc}(s)$, of PRCOT controlled boost converter is derived and well matches SIMPLIS simulation and experiment results for both constant slope and exponentially varying slope passive ramp cases. The proposed control strategy can be applied to various control schemes with varying modulation ramp slopes.

Acknowledgment

The authors would like to thank SIMPLIS Technologies Corporation, USA, for providing SIMPLIS simulation tool.

References

[1] F. Su and W. H. Ki, "Digitally assisted quasi-V2 hysteretic buck converter with fixed frequency and without using large-ESR capacitor," in *Proc. IEEE Int. Solid-State Circuits Conf. - Dig. Tech. Papers*, 2009, pp. 446–447.

[2] C. S. Huang, C. Y. Wang, J. H. Wang, and C. H. Tsai, "A fast-transient quasi-V2 switching buck regulator using AOT control," in *Proc. IEEE Asian Solid-State Circuits Conf.*, 2011, pp. 53–56.

[3] Y. C. Lin, C. J. Chen, D. Chen, and B. Wang, "A ripple-based constant on-time control with virtual inductor current and offset cancellation for DC power converters," *IEEE Trans. Power Electron.*, vol. 27, no. 10, pp. 4301–4310, Oct. 2012.

[4] C. H. Tsai, S. M. Lin, and C. S. Huang, "A fast-transient quasi-V^2 switching buck regulator using AOT control with a load current correction (LCC) technique," *IEEE Trans. Power Electron.*, vol. 28, no. 8, pp. 3949–3957, Aug. 2013.

[5] K. Y. Hu, S. M. Lin, and C. H. Tsai, "A fixed-frequency quasi-V^2 hysteretic buck converter with PLL-based two-stage adaptive window control," *IEEE Trans. Circuits Syst. I: Regular Papers*, vol. 62, no. 10, pp. 2565–2573, Oct. 2015.

[6] D. H. Jung, K. Kim, S. Joo, and S. O. Jung, "0.293-mm2 Fast transient response hysteretic quasi-V^2 DC–DC converter with area-efficient time-domain-based controller in 0.35-μm CMOS," *IEEE J. Solid-State Circuits*, vol. 53, no. 6, pp. 1844–1855, Jun. 2018.

[7] S. H. Pakala, P. R. Surkanti, and P. M. Furth, "A spread-spectrum mode enabled ripple-based buck converter using a clockless frequency control," *IEEE Trans. Circuits Syst. II, Exp. Briefs*, vol. 66, no. 3, pp. 382–386, Mar. 2019.

[8] M. G. Jeong, J. G. Kang, J. Park, and C. Yoo, "A current-mode hysteretic buck converter with multiple-reset RC-based inductor current sensor," *IEEE Trans. Ind. Electron.*, vol. 66, no. 11, pp. 8445–8453, Nov. 2019.

[9] C. Y. Ting, J. Y. Lin, and C. C. P. Chen, "A quasi-V2 hysteretic buck converter with adaptive COT control for fast DVS and load-transient response in RF applications," *IEEE Trans. Circuits Syst. II, Exp. Briefs*, vol. 67, no. 3, pp. 531–535, Mar. 2020.

[10] Y. C. Li, C. J. Chen, and C. J. Tsai, "A constant on-time buck converter with analog time-optimized on-time control," *IEEE Trans. Power Electron.*, vol. 35, no. 4, pp. 3754–3765, Apr. 2020.

[11] W. Huang, L. Liu, X. Liao, C. Xu, and Y. Li, "A 240-nA quiescent current, 95.8% efficiency AOT-controlled buck converter with A2-comparator and sleep-time detector for IoT application," *IEEE Trans. Power Electron.*, vol. 36, no. 11, pp. 12898–12909, Nov. 2021.

[12] Y. L. Chao, C. J. Tsai, and C. J. Chen, "A 4-MHz ultra-fast transient response capacitor current adaptive on-time (CCAOT) controlled buck converter with passive ramp compensation," in *Proc. Int. Power Electron. Conf.*, 2022, pp. 1511–1516.

[13] Y. L. Huang, C. J. Chen, C. C. Hsu, and T. W. Huang, "Peak passive ripple mode control for boost converter with fast transient response," in *Proc. IEEE 7th Southern Power Electron. Conf.*, 2022, pp. 1–6.

[14] Y. Y. Lin, C. J. Chen, Y. C. Lin, and T. W. Huang, "A bidirectional three-level converter with single point sensing technique for flying capacitor balance," in *Proc. IEEE Appl. Power Electron. Conf. Expo.*, 2022, pp. 681–686.

[15] H. H. Chen, C. J. Tsai, and C. J. Chen, "A monolithic 30uA –1.5A >85%-efficiency, passive-ramp-extended-ton controlled buck converter for mobile SoC fast DVS," in *Proc. IEEE Appl. Power Electron. Conf. Expo.*, 2023, pp. 1211–1216.

[16] C. Y. Wu, C. J. Tsai, C. J. Chen, C. C. Tu, S. T. Wang, and Y. H. Wen, "A 200 nA quiescent current N-FinFET power stage buck converter with passive ramp on-off-time control in 12 nm FinFET," in *Proc. Int. VLSI Symp. Technol., Syst. Appl.*, 2023, pp. 1–4.

[17] Y. R. Huang, C. J. Chen, J. C. Wu, and T. W. Huang, "A fast-transient boost converter with peak passive ripple mode control and AC couple," *IEEE Trans. Power Electron.*, vol. 38, no. 10, pp. 12975–12987, Oct. 2023.

[18] J. Li and F. C. Lee, "New modeling approach and equivalent circuit representation for current-mode control," *IEEE Trans. Power Electron.*, vol. 25, no. 5, pp. 1218–1230, May 2010.

[19] J. Li and F. C. Lee, "Modeling of V2 current-mode control," in *Proc. 24th Annu. IEEE Appl. Power Electron. Conf. Expo.*, 2009, pp. 298–304.

[20] C. F. Nien et al., "A novel adaptive quasi-constant on-time current-mode buck converter," *IEEE Trans. Power Electron.*, vol. 32, no. 10, pp. 8124–8133, Oct. 2017.

[21] L. Kong, D. Chen, S. F. Hsiao, C. F. Nien, C. J. Chen, and K. F. Li, "A novel adaptive-ramp ripple-based constant on-time buck converter for stability and transient optimization in wide operation range," *IEEE J. Emerg. Sel. Topics Power Electron.*, vol. 6, no. 3, pp. 1314–1324, Sep. 2018.

[22] S. Bari, Q. Li, and F. C. Lee, "High frequency small signal model for inverse charge constant on-time (IQCOT) control," in *Proc. IEEE Energy Convers. Congr. Expo.*, 2018, pp. 6000–6007.

[23] C. H. Cheng, C. J. Chen, and S. S. Wang, "Small-signal model of flyback converter in continuous-conduction mode with peak-current control at variable switching frequency," *IEEE Trans. Power Electron.*, vol. 33, no. 5, pp. 4145–4156, May 2018.

[24] W. C. Liu, C. J. Chen, C. H. Cheng, and H. J. Chen, "A novel accurate adaptive constant on-time buck converter for a wide-range operation," *IEEE Trans. Power Electron.*, vol. 35, no. 4, pp. 3729–3739, Apr. 2020.

[25] S. F. Hsiao, C. F. Nien, D. Chen, and C. J. Chen, "Four-frequency small-signal model for high-bandwidth voltage regulator with current-mode control," *IEEE Access*, vol. 10, pp. 25633–25644, 2022.

[26] X. Cheng, J. Liu, Y. Shao, and Z. Liu, "High-frequency modelling of constant on-time current mode buck converter and controller design by combining genetic algorithm," *IEEE Trans. Power Electron.*, vol. 37, no. 12, pp. 15099–15110, Dec. 2022.

[27] D. Lu, X. Zeng, and Z. Hong, "Accurate loop gain model of ripple-based constant on-time controlled buck converters," *IEEE Trans. Power Electron.*, vol. 38, no. 6, pp. 7034–7048, Jun. 2023.

[28] Y. Huang and C. Cheung, "Small signal modeling of the hysteretic modulator with a current ripple synthesizer," in *Proc. IEEE Appl. Power Electron. Conf. Expo.*, 2016, pp. 1616–1623.
[29] Y. C. Hsu, D. Chen, S. F. Hsiao, H. Y. Cheng, and C. S. Huang, "Modeling of the control behavior of current-mode constant on-time boost converters," *IEEE Trans. Ind. Appl.*, vol. 52, no. 6, pp. 4919–4927, Nov. 2016.
[30] R. W. E. A. D. Maksimovic, *Fundamentals Power Electron*, 2nd ed. Norwell, MA, USA: Kluwer, 2001.

Yi-Rong Huang received the B.S. degree in electric engineering from the Department of Electrical Engineering, National Chiao Tung University, Hsinchu, Taiwan, in 2015, and the M.S. degree in power electronic from Graduate Institute of Electrical Engineering, National Taiwan University, Taipei, Taiwan, in 2017.

From 2017 to 2018, he was an Electric Engineer, Garmin Corporation, Taoyuan, Taiwan. From 2019 to 2020, he was an Engineer with IC Research and Development Department, Richtek Technology Corporation, Hsinchu, Taiwan.

His current research interests include control, modeling, and power IC design.

Ching-Jan Chen (Senior Member, IEEE) received B.S. and Ph.D. degrees in electrical engineering from National Taiwan University, Taipei, Taiwan, in 2006 and 2011, respectively.

From 2010 to 2011, he was a Visiting Scholar with the Center of Power Electronic Systems (CPES) of Virginia Tech., Blacksburg, VA, USA. From 2011 to 2015, he was a Senior IC research and a Development Engineer with Richtek Technology Corporation, Hsinchu, Taiwan, which is Asia No. 1 fabless power IC company and CPU Power IC supplier according to revenue. His work was focused on new control scheme development and IC design of the voltage regulator controller for CPU power. In February 2015, he was an Assistant Professor with the Department of Electrical Engineering, National Taiwan University, Taiwan, where he is currently an Associate Professor.

His current research interests include control, modeling, and power IC design of dc–dc and ac-dc power converters for CPU and mobile devices, and GaN/SiC driver IC design.

Dr. Chen is a Senior Member of the IEEE Power Electronics Society. He is the recipient of 2016 Young Researcher Award from the Electrical Power Engineering Division, Ministry of Science and Technology, Taiwan, 2020 Outstanding Teaching Award from NTU, 2020 Research Contribution Award from NTU EECS, 2021 Ta-You Wu Memorial Award from MOST, Taiwan, and 2023 Delta Young Technology Scholar Award (Power Electronics). He is the co-recipient of 2019 IEEE Transportation Electrification Conference Asia-Pacific (ITEC-AP) Best Paper Award and 2018 International Workshop on Power Supply on Chip (PwrSoC) Best Poster Award. He served more than 20 times as session chair, topic chair, and financial chair in several IEEE conferences and competitions, such as ECCE, ECCE-Asia, International Future Energy Challenge, IFEEC, WiPDA Asia, ITEC-Asia Pacific, and VLSI-DAT. He is the Secretary, vice-chair, and then chair of the IEEE PELS Taipei Chapter from 2018 till now and also the recipient of IEEE PELS Best Chapter Award in 2018. He is an Associate Editor for IEEE TRANSACTIONS ON POWER ELECTRONICS.